



Direct generation of hydroxyl radicals over bismuth oxybromide nanobelts with tuned band structure for photocatalytic pollutant degradation under visible light irradiation

Chu-Ya Wang¹, Xing Zhang¹, Ying-Jie Zhang, Jie-Jie Chen*, Gui-Xiang Huang, Jun Jiang, Wei-Kang Wang, Han-Qing Yu*

CAS Key Laboratory of Urban Pollutant Conversion, Department of Chemistry, University of Science & Technology of China, Hefei, 230026, China



ARTICLE INFO

Keywords:
 $\text{Bi}_{24}\text{O}_{31}\text{Br}_{10}$ nanobelt
 Band structure
 Hydroxyl radical
 Bisphenol A
 Photocatalysis

ABSTRACT

Various photocatalysts have been fabricated and tested for the treatment of water and wastewater. As visible-light-driven photocatalysts, bismuth oxybromide nanomaterials have weak responses to visible light and low activities of using photogenerated h^+ to produce hydroxyl radicals ($\cdot\text{OH}$), both of which are limited by their band structures. Thus, modification of bismuth oxybromide to form an optimized band structure is essential to enhance its photocatalytic activity for environmental applications. In this work, an oxygen-rich bismuth oxybromide nanomaterial, $\text{Bi}_{24}\text{O}_{31}\text{Br}_{10}$ nanobelt, was fabricated using a solvothermal method, which possessed a narrower band gap and a more positive position of valence band top. As a result, this catalyst exhibited a strong response to visible light and produced large quantities of $\cdot\text{OH}$ directly via its photogenerated h^+ , which contributed to the outstanding performance of photocatalysis, as evidenced by the experimental results and density functional theoretical (DFT) calculations. Under visible light irradiation, the $\text{Bi}_{24}\text{O}_{31}\text{Br}_{10}$ nanobelt exhibited a substantially enhanced photocatalytic efficiency for the degradation of bisphenol A compared to those of $\text{Bi}_{24}\text{O}_{31}\text{Br}_{10}$ and BiOBr nanosheets. Moreover, this catalyst could resist most interfering ions and was able to treat two types of actual industrial wastewaters efficiently. This work elucidates a new approach to modify photocatalysts and is helpful to expand practical applications of photocatalytic technologies for water and wastewater treatment.

1. Introduction

Impacts of organic pollutants on environment and human beings have aroused great attentions [1,2]. Among various organic pollutants, Bisphenol A (BPA) is found to be a type of endocrine-disrupting chemical and refractory to commonly used water purification methods [3]. Photocatalytic technology is a green and efficient process to solve this problem [4–9]. Since bismuth oxyhalide nanomaterials, including BiOCl , BiOBr and BiOI , possess a special layered structure and $[\text{Bi}_2\text{O}_2]^{2+}$ layer is sandwiched by two $[\text{X}_2]^{2-}$ layers (Fig. S1), the static electric field between layers substantially promotes the separation and transportation of photogenerated excitons, which results in a high photocatalytic activity [10–16]. Since the wide band gap of BiOCl (3.4 eV) severely restricts its visible light absorption, BiOBr has a narrower band gap (2.7 eV) and is more suitable for practical applications [17–28]. However, the absorption edge of BiOBr just occurs at the boundary of visible light and UV light (420 nm), resulting in its low

efficiency of visible light utilization. Furthermore, the valence band (VB) top position of BiOBr is not sufficiently positive compared to the oxidation potential of $\text{OH}^-/\cdot\text{OH}$ (2.38 eV), suggesting that photogenerated h^+ on BiOBr VB are unable to directly produce hydroxyl radical ($\cdot\text{OH}$), which is a key free radical for decontamination [1,10,29,30].

Previous works have demonstrated that changing the morphology of BiOBr nanomaterial and adjusting the ratio of O and Br through oxygen-rich modification can optimize the band structure [31–34]. In most cases, one-dimensional (1D) nanostructures such as nanobelt can exhibit a higher photocatalytic activity because of its higher exposure of active sites [35]. The band structures of oxygen-rich bismuth oxybromide nanomaterials can be efficiently tuned via changing the ratio of Bi, O and Br [33]. Some oxygen-rich bismuth oxybromide nanomaterials and heterojunctions with different morphologies, including $\text{Bi}_{24}\text{O}_{31}\text{Br}_{10}$ nanosheets with controllable thickness, $\text{Bi}_{24}\text{O}_{31}\text{Br}_{10}$ with three-dimensional morphology, $\text{BiOBr}/\text{Bi}_{24}\text{O}_{31}\text{Br}_{10}$ heterojunction,

* Corresponding authors.

E-mail addresses: chenjie@ustc.edu.cn (J.-J. Chen), hqyu@ustc.edu.cn (H.-Q. Yu).

¹ These authors contributed equally to this work.

$\text{Bi}_{12}\text{O}_{17}\text{Cl}_2/\text{Bi}_{24}\text{O}_{31}\text{Br}_{10}$ heterojunction and $\text{Bi}_{24}\text{O}_{31}\text{Cl}_x\text{Br}_{10-x}$ solid solution, have been synthesized and their improved photocatalytic capacities have been demonstrated [36–39]. However, in most cases, e.g., for the $\text{Bi}_{24}\text{O}_{31}\text{Br}_{10}$ nanosheets reported previously [36], despite the narrowed band gap, the VB top position is not sufficiently positive for the direct generation of $\cdot\text{OH}$ yet. Therefore, the photocatalytic pollutant degradation may mainly rely on the direct oxidation by h^+ rather than free radicals, which leads to the low mineralization efficiency. Furthermore, cetyltrimethyl ammonium bromide is commonly used as a surfactant to synthesize BiOBr , but it is easy to be chemically adsorbed on the product surface, which shields active sites and causes negative effect to the catalytic performance [2,36].

In this work, a novel oxygen-rich $\text{Bi}_{24}\text{O}_{31}\text{Br}_{10}$ nanomaterial with a 1D belt-like structure was synthesized through a simple solvothermal route. The as-prepared $\text{Bi}_{24}\text{O}_{31}\text{Br}_{10}$ nanobelts was used to degrade BPA under visible light irradiation. Moreover, intermediates were identified and a possible degradation pathway of BPA degradation by the catalyst was proposed. In addition, impacts of some widely present interfering ions (SO_4^{2-} , Cl^- , NO_3^- , PO_4^{3-} and CO_3^{2-}) on the photocatalytic degradation were evaluated, and the feasibility of using the catalysts for the treatment of two types of actual industrial wastewaters was investigated. Also, the photochemical and electrochemical characteristics of the nanobelts were examined in order to confirm the modification of band structure. Then, its ability to generate $\cdot\text{OH}$ under visible light irradiation and the corresponding generation pathway were evaluated. Based on the results of density functional theoretical (DFT) calculation, the band structure-mediated photocatalytic performance of the $\text{Bi}_{24}\text{O}_{31}\text{Br}_{10}$ nanobelts for pollutant degradation were elucidated.

2. Experimental section

2.1. Fabrication of $\text{Bi}_{24}\text{O}_{31}\text{Br}_{10}$ nanobelts

All chemicals with analytical grade were bought from Shanghai Chemical Co., China, and directly used. $\text{Bi}(\text{NO}_3)_3 \cdot 5\text{H}_2\text{O}$ of 2 mmol was dosed into 10-mL ethylene glycol (EG). After 15-min sonication, $\text{Bi}(\text{NO}_3)_3 \cdot 5\text{H}_2\text{O}$ was also dosed into EG, forming a colorless and homogeneous solution. NH_4Br of 2 mmol was dissolved in distilled water of 25 mL to prepare a homogeneous solution under vigorous stirring. With stirring, NH_4Br solution was added into the $\text{Bi}(\text{NO}_3)_3$ solution, and a suspension was formed quickly. After that, 0.7 mL of ethanol amine was added under stirring for additional 10 min. Then, all the reactants were transferred into an autoclave for solvothermal reaction at 160 °C for 12 h. After the reaction was completed and cooled down, the solid product was obtained and washed via centrifugation using distilled water and alcohol. Thereafter, a 12-h vacuum drying process at 80 °C was adopted to remove the residual water and alcohol in the product. As a comparison, BiOBr was also prepared using the same procedure without ethanol amine, and the $\text{Bi}_{24}\text{O}_{31}\text{Br}_{10}$ nanosheets were synthesized as reported previously [36].

2.2. Physicochemical characterization

The X-ray powder diffraction (XRD) patterns of the samples were characterized using a Philips X' Pert PRO SUPER diffractometer equipped with graphite monochromatized Cu $\text{K}\alpha$ radiation ($\lambda = 1.541874 \text{ \AA}$). In order to observe the morphologies of the products, a JSM-6700 F field emission scanning electron microscope (SEM) equipped with an X-650 scanning electron micro analyzer (JEOL Co., Japan) and a transmission electron microscope (TEM) (H-7650, Hitachi Co., Japan) with an acceleration voltage of 200 kV were used. The high-resolution transmission electron microscope (HRTEM), selected area electron diffraction (SAED), and the element mapping were obtained using a scanning transmission electron microscope (STEM) (JEM-ARM200F, JEOL Co., Japan), and the acceleration voltage was also

200 kV. The X-ray photoelectron spectroscopy (XPS) tests were performed using an electron spectroscopy (ESCALAB250, Thermo Fisher Inc., USA) in order to detect the chemical composition and the VB top position of the samples. The optical properties of the samples were analyzed based on the diffuse reflectance spectrum (DRS), which were taken from a UV-vis spectrophotometer (Solid 3700, Shimadzu Co., Japan). On the basis of Brunauer-Emmett-Teller (BET) method, a Builder 4200 instrument (Tristar II 3020 M, Micromeritics Co., USA) was used to measure the surface areas of the samples.

2.3. Photocatalytic BPA degradation experiments

BPA was used as the target organic pollutant to examine the photocatalytic capacities of the prepared catalysts. A Xe arc lamp (500 W) and a visible light cutoff filter (420 nm) were used to eliminate UV light. The BPA concentration in the raw solution was 10 mg L^{-1} . Before irradiation, 10 mg of the catalyst was dosed into 30 mL BPA solution. To achieve an adsorption/desorption equilibrium, the solution was stirred for 30 min before irradiation. In the interference tests, various ions including SO_4^{2-} , Cl^- , NO_3^- , PO_4^{3-} and CO_3^{2-} at a concentration of 100 mg L^{-1} were individually added into the BPA solution. At pre-determined time intervals, 1 mL of solution was collected as the sample and centrifuged immediately to remove the particles for analysis.

The BPA concentration was measured using a high performance liquid chromatography (HPLC, 1260 Infinity, Agilent Co., USA) as described previously.² The intermediate products in the photocatalysts were analyzed with a gas chromatography-mass spectrometry (GC-MS) (7890B GC System and 5977B MDS, Agilent Co., USA). The working conditions of GC-MS are given in *Supporting Information*. The mineralization efficiency of the catalysts was evaluated through measuring the solution total organic carbon (TOC) concentrations (Muti N/C 2100, Analytik Co., Germany). The generated free radicals in the photocatalysis was detected using an electron spin resonance (ESR) (JES-FA200, JEOL Co., Japan), and 5,5-dimethyl-1-pyrroline N-oxide (DMPO) was used to trap the generated $\cdot\text{OH}$ and $\cdot\text{O}_2$ in aqueous and methanol dispersions respectively. Also, the generated $\cdot\text{OH}$ and $\cdot\text{O}_2$ were detected using terephthalic acid (TPA) and nitrotetrazolium blue chloride (NBT), respectively.

Moreover, two actual industrial wastewaters, i.e., soybean-processing wastewater and winery wastewater, were collected to investigate the mineralization efficiency of the prepared photocatalyst. More details about the two wastewaters and degradation tests are provided in *Supplementary Material* and Table S1. The dosage of the photocatalyst was 1 g L^{-1} .

2.4. Electrochemical tests

A three-electrode system was used to carry out all electrochemical experiments.² The glass carbon loaded with the catalyst sample was used as the working electrode for electrochemical impedance spectroscopy (EIS) and Mott-Schottky tested. In the photocurrent test, a fluorine-doped tin oxide (FTO) conductive glass was used to load the catalyst sample, whereas Pt wire and Ag/AgCl (KCl, 3 M) electrodes were adopted as the counter and reference electrodes respectively. The EIS test was carried out in 0.05 M $\text{K}_3[\text{Fe}(\text{CN})_6]$ and $\text{K}_4[\text{Fe}(\text{CN})_6]$ solution at an applied voltage of 0.3 V, voltage amplitude of 5 mV and alternating current frequency in a range of 10^6 to 10^{-2} Hz. The Mott-Schottky plot was calculated with the impedance measurement, which was conducted in 0.1 M Na_2SO_4 solution at a frequency of 1 kHz and an applied voltage range of 0.3–1.0 V. The photocurrent test was conducted in 0.1 M Na_2SO_4 aqueous solution using the amperometric *i-t* curve method at a bias voltage of 0.22 V for 550 s. A potentiostat (CHI 660E, CH Instrument Co., China) was used to conduct these above electrochemical measurements, and the aforementioned light source in the photocatalytic test was also used for the photocurrent test.

2.5. DFT calculations

The crystal structures of BiOBr and the oxygen-rich $\text{Bi}_{24}\text{O}_{31}\text{Br}_{10}$ were characterized by XRD phase analysis as P4/nmm S1 tetragonal and A12/m1 monoclinic space groups, respectively. The optimized lattice parameters for the crystal models of BiOBr ($a = b = 3.92 \text{ \AA}$, $c = 8.076 \text{ \AA}$) and $\text{Bi}_{24}\text{O}_{31}\text{Br}_{10}$ ($a = 10.13 \text{ \AA}$, $b = 4.01 \text{ \AA}$, $c = 29.97 \text{ \AA}$, $\beta = 90.15^\circ$) are consistent well with the experimental measurements. As shown in Fig. S2, periodic surface slabs with 15 \AA vacuum regions between the slabs were used both for the (001) surface of the BiOBr nanosheets and the (117) surface of the nanobelts [40]. First-principles DFT calculations were performed with the periodic plane-wave pseudopotential approach as implemented in the CASTEP code [41]. The exchange-correlation energy and potential were described by using the generalized gradient approximation (GGA) of the Perdew-Burke-Ernzerhof (PBE) functional [42]. The cut-off energy and self-consistent field (SCF) tolerance were set at 340 eV and $1.0 \text{ e}^{-4} \text{ eV}/\text{cell}$, respectively. The initial geometry configurations were optimized by Broyden, Fletcher, Golfarb and Shannom (BFGS) algorithm [43]. The Brillouin zone was sampled by the Monkhorst-Pack grid with k point spacing being maintained not more than 0.07 \AA^{-1} . After geometric optimization, the electronic band structures and the density of states (DOS) were calculated.

3. Results and discussion

3.1. Morphology and structural characteristics of $\text{Bi}_{24}\text{O}_{31}\text{Br}_{10}$ nanobelts

The powder XRD was used to identify the phase and confirm the crystal structure of the product. Fig. 1 shows that the diffraction peaks of the product were indexed to $\text{Bi}_{24}\text{O}_{31}\text{Br}_{10}$ (JCPDS card No. 75-0888), whose lattice parameters were 10.13 , 4.008 and 29.97 \AA for a–c, respectively. There were no signals of other crystals in the XRD pattern, implying that the product was composed of the single phase $\text{Bi}_{24}\text{O}_{31}\text{Br}_{10}$ with a high purity.

Apart from the XRD test, SEM, TEM and HRTEM were also used to characterize the morphology and structure of the products and the images are shown in Fig. 2. The SEM images (Fig. 2a and b) clearly show the homogeneous belt-like structure of the product with a mean length of several micrometers. The TEM image (Fig. 2c) also reveals the belt-like morphology of the nanobelts. The width of each nanobelt along its entire length was highly uniform with a mean width in a range of 100 – 400 nm . In the solvothermal procedure, ethanol amine (a typical alkali) was used to reduce Br element [36]. Moreover, it could also facilitate the growth speed along a specific direction and is helpful to the formation of the belt-like structure [2]. The HRTEM image was used to observe the crystal structure of the nanobelts (Fig. 2d). The high crystallinity of the nanobelts was confirmed by clear lattice fringes. The HRTEM image shows that the mean distance of the lattice fringes was

0.28 nm , which is theoretically in accordance with those of (117) and (1–17) facets in $\text{Bi}_{24}\text{O}_{31}\text{Br}_{10}$ with monoclinic phase, respectively. The measured angle between the atomic planes of (117) and (1–17) was close to 90° , which is consistent with the theoretical interfacial angle 89° . As labeled in the SAED pattern in Fig. 2d, the angle of the adjacent spots was measured as 89° , which theoretically matches the angle between the two facets of (117) and (1–17) in $\text{Bi}_{24}\text{O}_{31}\text{Br}_{10}$. Moreover, the EDS mapping result clearly reveals the uniform distributions of Bi, O and Br in the nanobelts (Fig. S3). As a comparison, the typical sheet structures of the $\text{Bi}_{24}\text{O}_{31}\text{Br}_{10}$ and BiOBr nanosheets could be clearly observed from their SEM and TEM images (Fig. S4).

XPS analysis was performed to examine the chemical states of the elements in the catalysts (Fig. 3). The C 1s peak was shifted to 284.60 eV in order to calibrate the experimental data of XPS test. Fig. 3a shows that the characteristic signals of the Bi, O and Br were clearly identified in the full scan spectrum. In the Bi 4f spectrum (Fig. 3b), there were two strong peaks with a splitting energy of 5.4 eV , which match the characteristic signals of $\text{Bi} 4f_{7/2}$ and $\text{Bi} 4f_{5/2}$ [1]. In Fig. 3c, the strong peak at 529.7 eV is in accordance with the lattice oxygen in the nanobelts, and the peak at 530.8 eV (the blue line) represents the hydroxyl groups on the surface of the sample [36,44,45]. Similarly, the two main peaks at 67.9 and 69.4 eV in the Br 3d spectrum (Fig. 3d) matched the characteristic signals of $\text{Br} 3d_{5/2}$ and $\text{Br} 3d_{3/2}$ well [36]. Therefore, the XPS results clearly reveal that the obtained products were composed of pure $\text{Bi}_{24}\text{O}_{31}\text{Br}_{10}$ nanobelts.

3.2. Photocatalytic degradation of BPA by $\text{Bi}_{24}\text{O}_{31}\text{Br}_{10}$ nanobelts

To evaluate the effectiveness of the prepared catalysts for BPA degradation, the photocatalytic experiments of the $\text{Bi}_{24}\text{O}_{31}\text{Br}_{10}$ nanobelts and $\text{Bi}_{24}\text{O}_{31}\text{Br}_{10}$ nanosheets, BiOBr nanosheets and TiO_2 (P25) were conducted (Fig. 4a). The blank test result shows that no BPA was removed, indicating that BPA was quite stable and could not be self-decomposed under the testing conditions. The BPA removal was very limited when TiO_2 (P25) was used, indicating its negligible response toward visible light. The $\text{Bi}_{24}\text{O}_{31}\text{Br}_{10}$ and BiOBr nanosheets had better performances than TiO_2 (P25), and approximately 25% and 40% of BPA were degraded within 120 min , respectively. The $\text{Bi}_{24}\text{O}_{31}\text{Br}_{10}$ nanosheets were more active than the BiOBr nanosheets. For the nanobelts, approximately 92% of BPA was removed after 120-min visible light irradiation. In addition to its great photocatalytic activity, the stability and reusability of the prepared nanobelts were also confirmed (Fig. S5).

In order to compare the photocatalytic activities of the photocatalysts in depth, their kinetic constants were calculated and the Langmuir-Hinshelwood model was used to fit the experimental data. Considering a very low concentration of the reactant in this system, the following pseudo first-order kinetic model was used:

$$-\ln(C_t/C_0) = kt \quad (1)$$

in which k is the apparent kinetic constant, while C_0 and C_t are the BPA concentrations before irradiation and at a given time t , respectively.

The calculated kinetics curves (Fig. S6) show that the experimental data matched well with the pseudo first-order kinetic model. The k values of the nanobelts, $\text{Bi}_{24}\text{O}_{31}\text{Br}_{10}$ nanosheets and BiOBr nanosheets were calculated to be 0.018 , 0.005 and 0.003 min^{-1} , respectively. Given that the exposure of active sites is essential to the photocatalytic performance, their BET surface areas were measured. Their calculated surface areas were 12.53 , 14.80 and $8.23 \text{ m}^2 \text{ g}^{-1}$ respectively and exhibited no substantial differences (Fig. S7). The surface-area-normalized kinetic constant of the $\text{Bi}_{24}\text{O}_{31}\text{Br}_{10}$ nanobelts was $1.44 \text{ mg min}^{-1} \text{ m}^{-2}$, which was much higher than those of the $\text{Bi}_{24}\text{O}_{31}\text{Br}_{10}$ nanosheets and BiOBr nanosheets (0.34 and $0.36 \text{ mg min}^{-1} \text{ m}^{-2}$ respectively). This confirms that the contribution of surface area to the enhanced

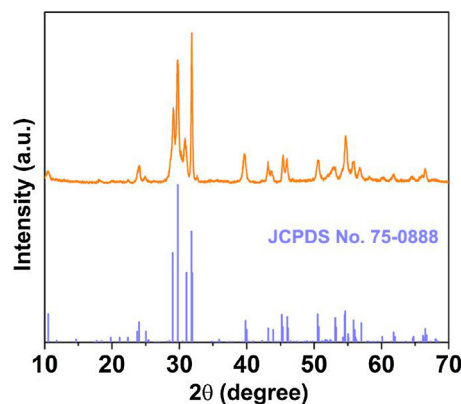


Fig. 1. XRD pattern of the $\text{Bi}_{24}\text{O}_{31}\text{Br}_{10}$ nanobelts.

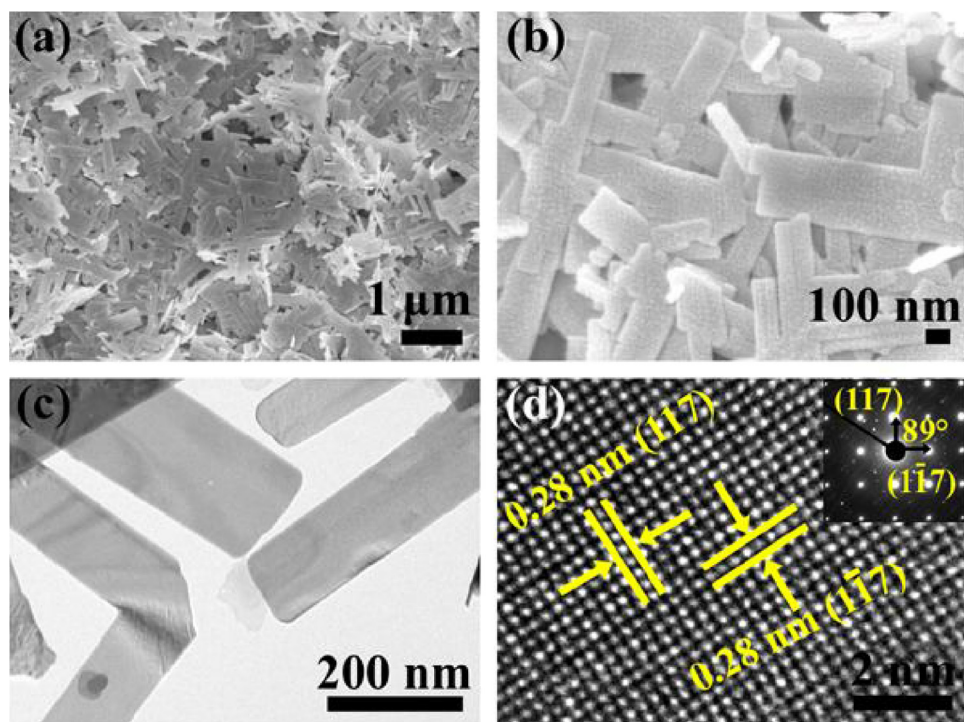


Fig. 2. (a) Low magnification and (b) high magnification SEM images, (c) TEM image and (d) HRTEM image of the $\text{Bi}_{24}\text{O}_{31}\text{Br}_{10}$ nanobelts. The SAED pattern is shown in the inset.

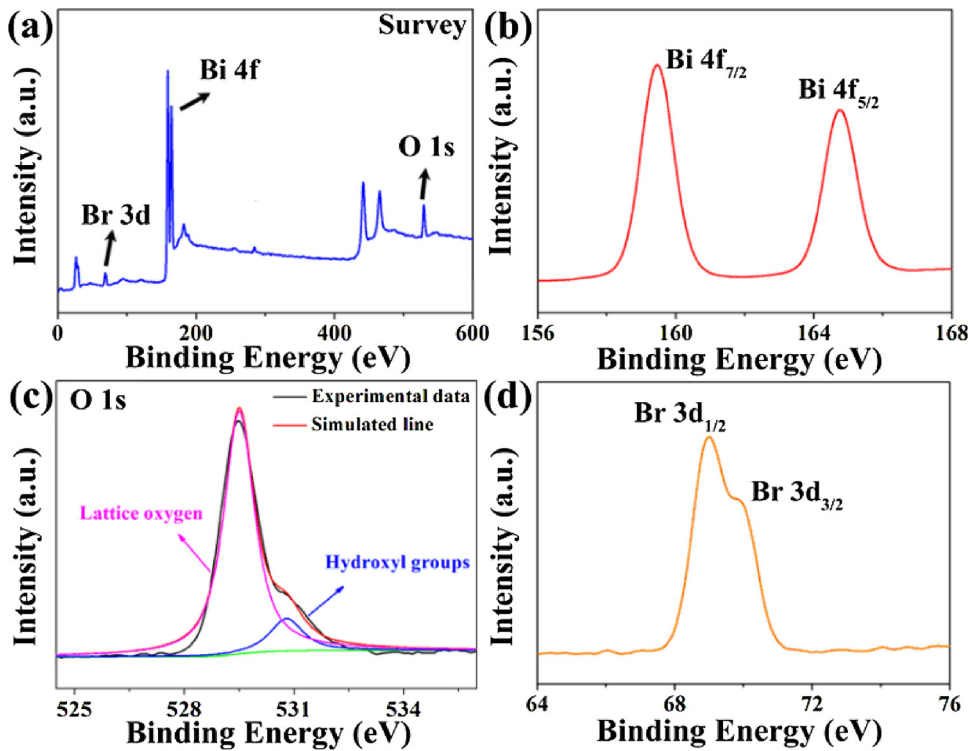


Fig. 3. XPS spectra of the $\text{Bi}_{24}\text{O}_{31}\text{Br}_{10}$ nanobelts: (a) survey XPS spectrum, (b) Bi 4f, (c) O1s, and (d) Br 3d.

photocatalytic performance of the nanobelts was negligible. Furthermore, the TOC removal in the BPA degradation over the nanobelts was also substantially higher than those of the two other catalysts (Fig. S8).

To further evaluate the potential of the $\text{Bi}_{24}\text{O}_{31}\text{Br}_{10}$ nanobelts for practical applications, series of photocatalytic degradation experiments in the presence of interfering ions were conducted. The dosage of each

ion was 100 mg L^{-1} , which was 10 times higher than that of BPA. As shown in Fig. 4b, the presence of Cl^- , NO_3^- , PO_4^{3-} and CO_3^{2-} , which are the most commonly present ions in aqueous environments, had negligible impacts on the BPA degradation by the nanobelts. Since sulfur compounds tend to poison Bi-based photocatalysts, the presence of SO_4^{2-} could inhibit the BPA degradation [17,46]. The photocatalytic degradation performance of the $\text{Bi}_{24}\text{O}_{31}\text{Br}_{10}$ nanobelts could be

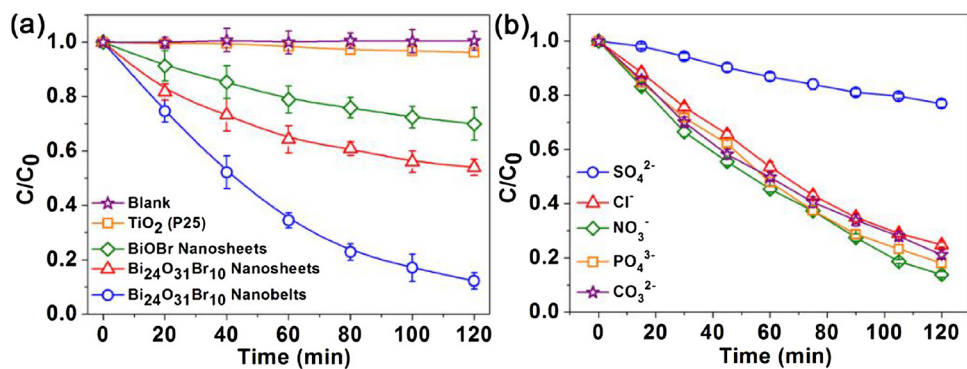


Fig. 4. (a) Photocatalytic degradation of BPA on the Bi₂₄O₃₁Br₁₀ nanobelts, Bi₂₄O₃₁Br₁₀ nanosheets, BiOBr nanosheets, TiO₂ (P25) and blank test and (b) photocatalytic degradation of BPA on the Bi₂₄O₃₁Br₁₀ nanobelts in the presence of SO₄²⁻, Cl⁻, NO₃⁻, PO₄³⁻ and CO₃²⁻.

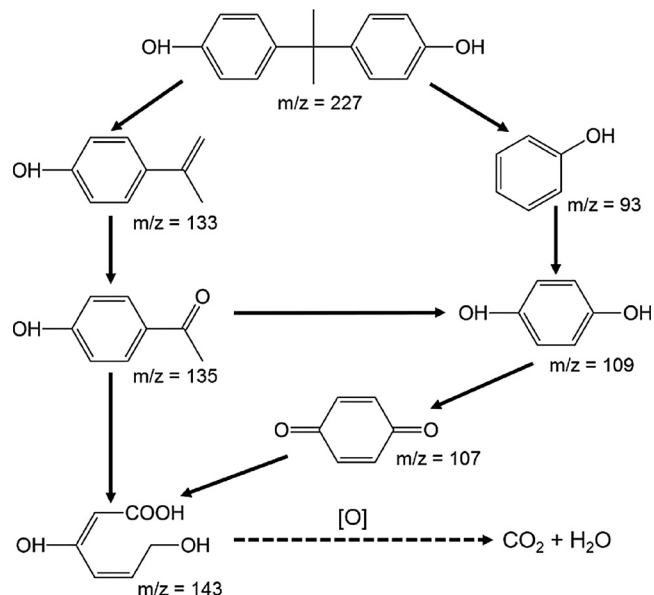


Fig. 5. Proposed photocatalytic BPA degradation pathway by the Bi₂₄O₃₁Br₁₀ nanobelts.

retained for practical water and wastewater treatment.

To gain insights into the BPA degradation pathway, the generated intermediates were identified using GC-MS and the result is shown in Fig. S9 and Table S1. With these results, the BPA photocatalytic degradation pathway by the Bi₂₄O₃₁Br₁₀ nanobelts is proposed and shown in Fig. 5 [47,48]. The product ions at *m/z* 133 and 93 were assigned to the two original intermediates decomposed from BPA, which might be the first step of BPA degradation. Then, these intermediates were

further oxidized (*m/z* 135, 109 and 107) until the benzene ring structure was broken, and the product ion at *m/z* 143 was considered as the aromatic ring opening product. Finally, these intermediates were oxidized in depth and mineralized into H₂O and CO₂.

3.3. Treatment of actual industrial wastewaters by Bi₂₄O₃₁Br₁₀ nanobelts

Two types of actual industrial wastewaters, soybean-processing wastewater and winery wastewater, were used to test the mineralization ability of the Bi₂₄O₃₁Br₁₀ nanobelts, and the results are shown in Fig. 6. The raw wastewaters were diluted before the photocatalytic tests, and the measured TOC concentrations of the diluted soybean-processing wastewater and the winery wastewater were 76 and 86 mg L⁻¹, respectively. As shown in Fig. 6, approximately 47% and 38% of TOC in the soybean-processing wastewater and winery wastewater were removed by the nanobelts after 4-h visible light irradiation, which were substantially higher than those for Bi₂₄O₃₁Br₁₀ nanosheets, BiOBr nanosheets and TiO₂ (P25). This result implies that the nanobelts possessed an enhanced photocatalytic performance and have a potential for practical applications.

3.4. Band structure of Bi₂₄O₃₁Br₁₀ nanobelts

Since surface area was unimportant to the enhanced photocatalytic performance of the catalysts, the band structure of the Bi₂₄O₃₁Br₁₀ nanobelts was recognized to be responsible for their superior photocatalytic degradation performance, because the redox potentials of photogenerated excitons are governed directly by the band structure. Herein, the band structure of the Bi₂₄O₃₁Br₁₀ nanobelts was measured using UV-vis DRS and XPS valence band spectrum with the two other catalysts as a comparison (Fig. 7). Although BiOBr is a visible-light-driven photocatalyst, its absorption edge occurs just at the boundary of visible light and UV light (420 nm), indicating its poor response to

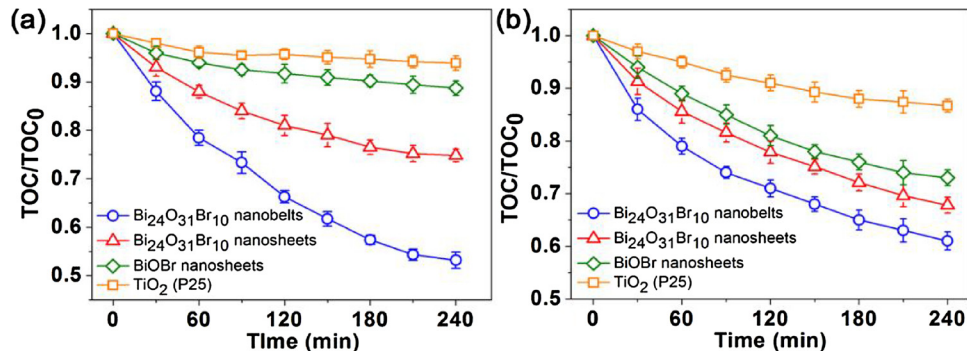


Fig. 6. Photocatalytic mineralization of (a) soybean-processing wastewater and (b) winery wastewater using the Bi₂₄O₃₁Br₁₀ nanobelts, Bi₂₄O₃₁Br₁₀ nanosheets, BiOBr nanosheets and TiO₂ (P25).

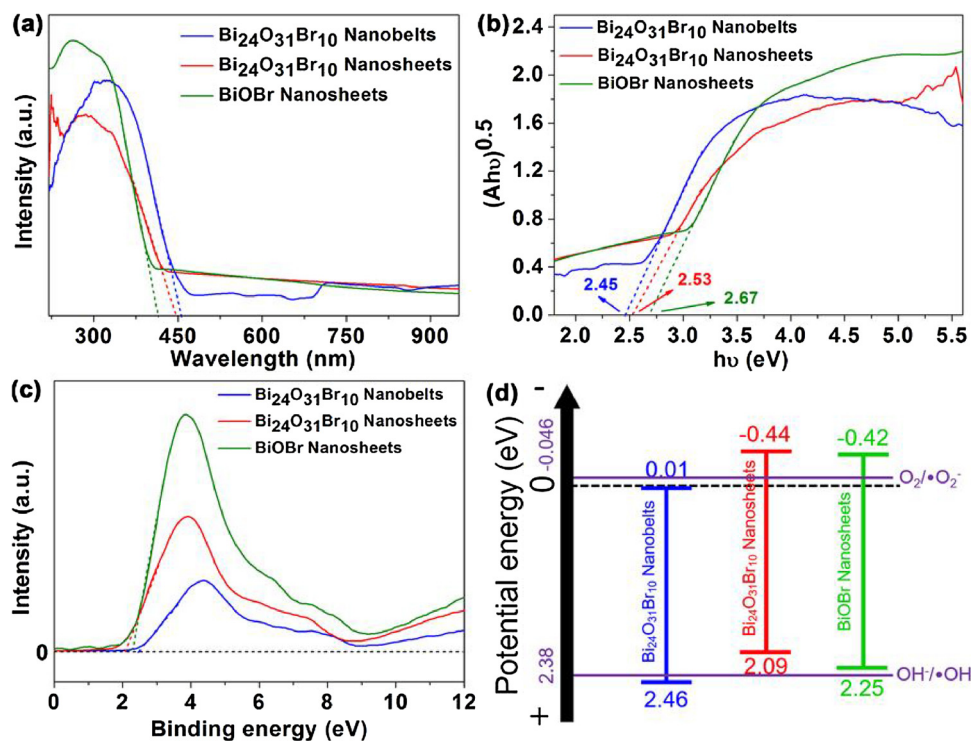


Fig. 7. (a) UV-vis diffuse reflectance spectra, (b) the band gap values, estimated from the plotted curve of $(Ahv)^{0.5}$ versus $h\nu$, (c) XPS valence band spectra, and (d) band structures of the three photocatalysts.

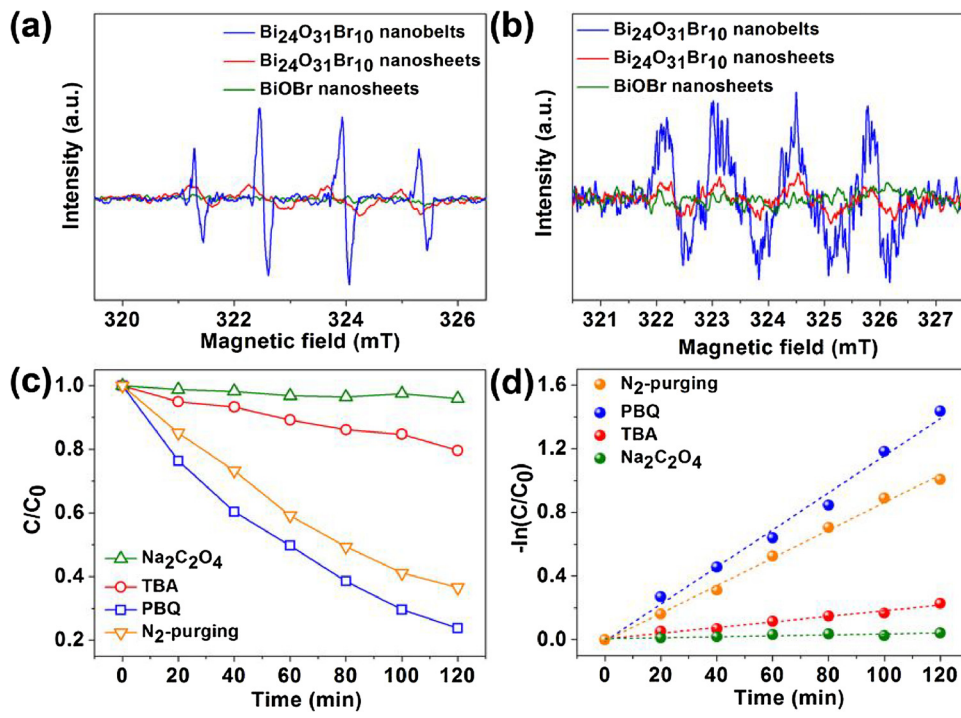


Fig. 8. (a) ESR signals of DMPO·OH in aqueous dispersion and (b) DMPO·O₂⁻ in methanol dispersion by the three photocatalysts, (c) photocatalytic BPA degradation over the Bi₂₄O₃₁Br₁₀ nanobelts by adding various scavengers and N₂-purging treatment, and (d) the corresponding kinetic curves.

visible light. However, after oxygen-rich treatment, the Bi₂₄O₃₁Br₁₀ nanobelts and nanosheets showed their absorption edge at approximately 450 nm (Fig. 7a), confirming their good solar light absorption capacity.

The light absorption of a semiconductor photocatalyst depends highly on its band gap, which can be calculated using the following equation [2]:

$$\alpha(hv) = A(hv - E_g)^{n/2} \quad (2)$$

in which E_g is band gap, $h\nu$ is photon energy, and α and A are absorption coefficient and light absorbance, respectively. The n value relies on the characteristics of the transition. In this work, n is 4 as the Bi₂₄O₃₁Br₁₀ is an indirect bandgap semiconductor.

In order to estimate the E_g value, the UV-vis DRS results of the photocatalysts were further processed and turned into Tauc plots (Fig. 7b). The calculated band gaps of the Bi₂₄O₃₁Br₁₀nanobelts and Bi₂₄O₃₁Br₁₀ nanosheets were 2.45 and 2.53 eV respectively, both of which were narrower than that of the BiOBr nanosheets (2.67 eV).

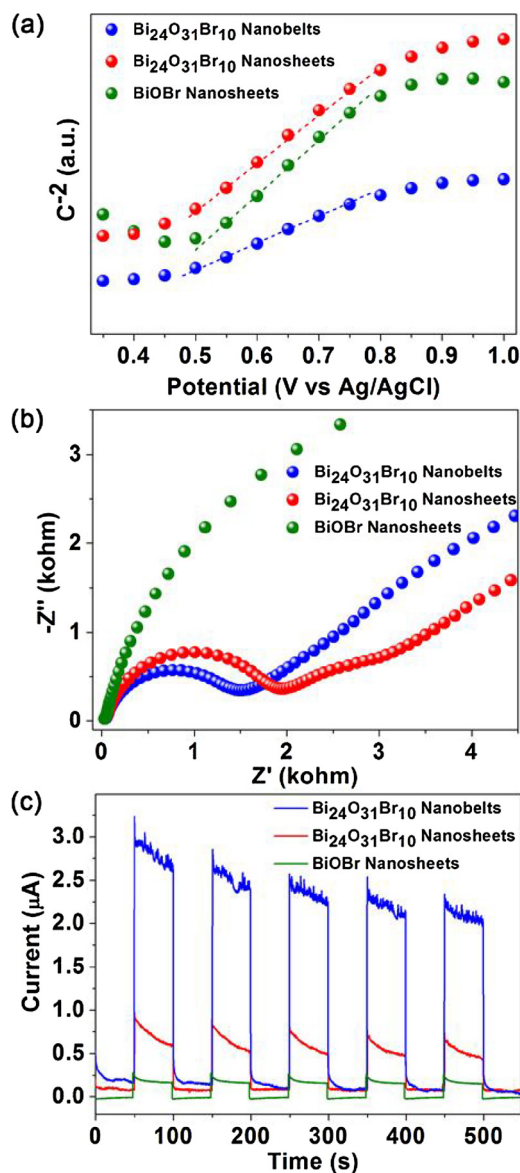


Fig. 9. (a) Mott-Schottky plots, (b) EIS Nyquist spectra, and (c) photocurrent responses of the three photocatalysts.

However, the VB top position of the $\text{Bi}_{24}\text{O}_{31}\text{Br}_{10}$ nanobelts (2.46 eV) was more positive than that of the $\text{Bi}_{24}\text{O}_{31}\text{Br}_{10}$ nanosheets (2.09 eV), (Fig. 7c), indicating that the nanobelts possessed a stronger oxidizing ability than the nanosheets. Compared with the HRTEM image of the $\text{Bi}_{24}\text{O}_{31}\text{Br}_{10}$ nanosheets in our previous work [36], the facet exposures of the $\text{Bi}_{24}\text{O}_{31}\text{Br}_{10}$ nanobelts was different. This might cause the positive-shift of the VB top position and result in a tailored band structure of the $\text{Bi}_{24}\text{O}_{31}\text{Br}_{10}$ nanobelts [49,50]. In addition, the conduction band (CB) bottom position can be obtained with the following equation:

$$E_g = E_{\text{VB}} - E_{\text{CB}} \quad (3)$$

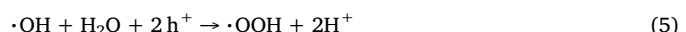
where E_{CB} is CB bottom position and E_{VB} is VB top position.

The band structures of the catalysts were calculated (Fig. 7d) [30,51]. The band gap of the $\text{Bi}_{24}\text{O}_{31}\text{Br}_{10}$ nanobelts was the narrowest, confirming its strongest response to visible light. Furthermore, it should be noted that only the VB top of the nanobelts was more positive than the oxidation potential of $\text{OH}^-/\cdot\text{OH}$ (2.38 eV). This indicates that the nanobelts could directly generate $\cdot\text{OH}$ via the holes (h^+) on VB, which is essential to its photocatalytic pollutant degradation capacity under visible light irradiation.

3.5. Free radicals formed in the photocatalytic degradation

In a typical photocatalytic system, mostly, organic molecules are degraded and mineralized by reactive oxygen radicals (ROS) that are generated by photocatalysts. Thus, the amount of the generated ROS and the generation pathway greatly affect the photocatalytic performance of a catalyst. As aforementioned, the $\text{Bi}_{24}\text{O}_{31}\text{Br}_{10}$ nanobelts possessed an optimized band structure, which might result in a more efficient ROS generation under visible light irradiation. Thus, in order to evaluate the impacts of band structure modification, ESR analysis was used to detect the generated ROS over the nanobelts, and the contribution of each ROS to the BPA degradation was measured by dosing various scavengers.

Two typical ROS, $\cdot\text{OH}$ and $\cdot\text{O}_2^-$, were detected in the ESR tests. The four peaks with the intensity of 1:2:2:1 can be ascribed to DMPO- $\cdot\text{OH}$ (Fig. 8a), while the four peaks with the same intensity are the signals of DMPO- $\cdot\text{O}_2^-$ (Fig. 8b) [52,53]. Also, the peak intensity highly relies on the concentration of the corresponding ROS. Thus, the high intensity of the ESR peaks produced by the nanobelts clearly indicates that it had a high activity to generate ROS under visible light irradiation. As a comparison, $\cdot\text{OH}$ and $\cdot\text{O}_2^-$ generated by the $\text{Bi}_{24}\text{O}_{31}\text{Br}_{10}$ nanosheets and BiOBr nanosheets were less because their peak intensities were very low. Moreover, TPA and NBT were also used to detect the generated $\cdot\text{OH}$ and $\cdot\text{O}_2^-$ respectively (Fig. S10), and the results were the same as those of the ESR tests [37,54]. Since the VB top position is more positive than the oxidation potential of $\text{OH}^-/\cdot\text{OH}$, it could be assumed that the nanobelts produce $\cdot\text{OH}$ directly with photogenerated h^+ , and $\cdot\text{O}_2^-$ is then generated from $\cdot\text{OH}$ via the following reactions [47,55]:



However, the $\text{Bi}_{24}\text{O}_{31}\text{Br}_{10}$ and BiOBr nanosheets reported in our previous studies produce $\cdot\text{OH}$ only indirectly with photogenerated e^- , because their VB top positions were more negative than that of $\text{OH}^-/\cdot\text{OH}$ [36]. Therefore, since the $\cdot\text{OH}$ -generating activity of the nanobelts was higher, its $\cdot\text{OH}$ -generating pathway was superior to those for the two other catalysts.

Photogenerated h^+ and ROS are active species commonly found in the decomposition of organic molecules. Herein, series of degradation experiments with using various scavengers were carried out to evaluate the contributions of different active species to BPA degradation. Sodium oxalate ($\text{Na}_2\text{C}_2\text{O}_4$), *tert*-butyl alcohol (TBA) and *p*-benzoquinone (PBQ) were used to scavenge h^+ , $\cdot\text{OH}$ and $\cdot\text{O}_2^-$ respectively, and N_2 -pruning was adopted to eliminate dissolved O_2 [2,36]. The results (Fig. 8c and d) show that the BPA degradation was substantially suppressed by dosing either $\text{Na}_2\text{C}_2\text{O}_4$ or TBA, indicating that $\cdot\text{OH}$ generated by h^+ was the main active species, and a fraction of h^+ could also oxidize BPA directly. However, the BPA degradations over the $\text{Bi}_{24}\text{O}_{31}\text{Br}_{10}$ nanosheets and BiOBr nanosheets mainly relied on the direct oxidation of h^+ (Fig. S11). As a result, the $\text{Bi}_{24}\text{O}_{31}\text{Br}_{10}$ nanobelts exhibited the best BPA degradation performance under visible light irradiation owing to its suitable band structure and the high efficiency of producing $\cdot\text{OH}$ as the reactive species.

3.6. Photoelectrical properties of $\text{Bi}_{24}\text{O}_{31}\text{Br}_{10}$ nanobelts

Apart from the band structure, the photoelectrical properties also affect the photocatalytic performance. Thus, the density of charge carrier, the efficiency of charge separation and the efficiency of charge conversion of the $\text{Bi}_{24}\text{O}_{31}\text{Br}_{10}$ nanobelts were measured and compared with those of the two other photocatalysts. The Mott-Schottky test

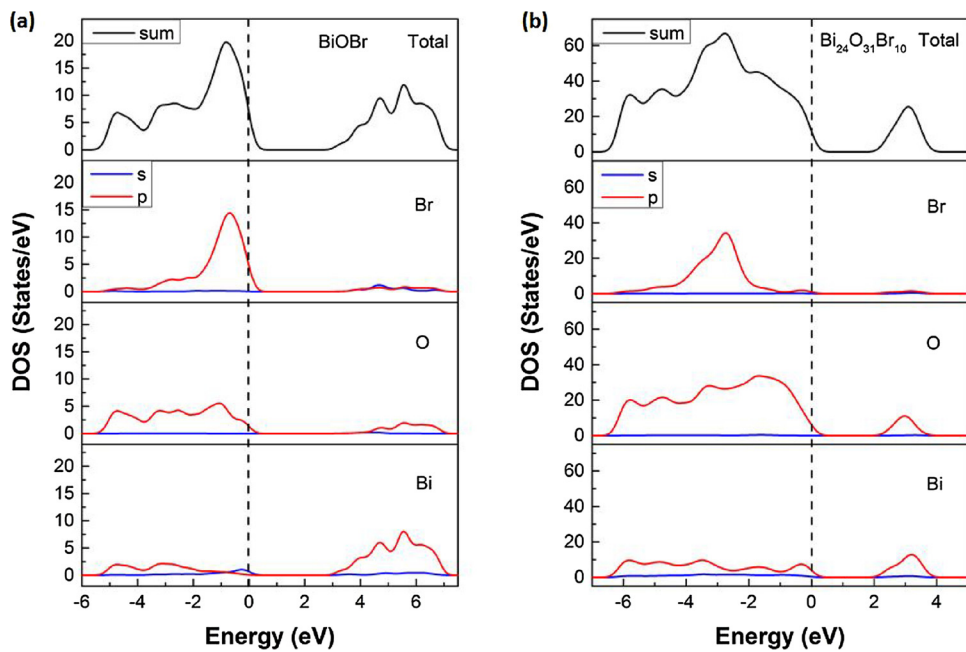


Fig. 10. DOS and PDOS of (a) the BiOBr (001) facet and (b) the $\text{Bi}_{24}\text{O}_{31}\text{Br}_{10}$ (117) facet, the dashed lines represent the Fermi level at 0 eV.

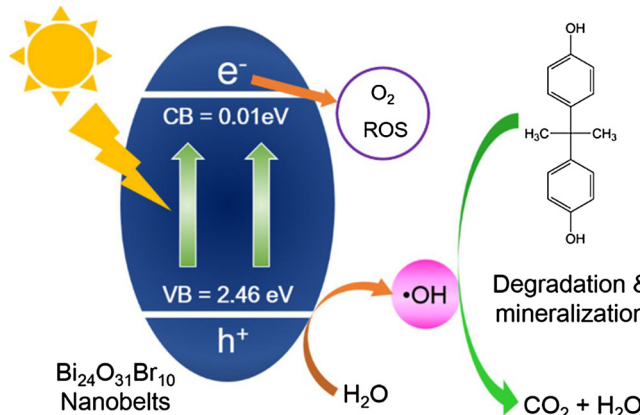


Fig. 11. Schematic of photocatalytic BPA degradation over $\text{Bi}_{24}\text{O}_{31}\text{Br}_{10}$ nanobelts.

results are shown in Fig. 9a. Obviously, the slopes of the three photocatalysts in the liner parts of Mott-Schottky curves were positive, indicating that they were *n*-type semiconductors. It is reported that the slope of the Mott-Schottky curve is reciprocal to the density of charge carrier [36]. The slope of the nanobelts was the smallest among the three catalysts, confirming that the charge carrier density of the $\text{Bi}_{24}\text{O}_{31}\text{Br}_{10}$ nanobelts was enhanced, which is in favor of its photocatalytic activity.

The effective charge separation also plays an important role in photocatalysis. Thus, EIS analysis of the three catalysts was performed (Fig. 9b). The enhancement of the charge separation efficiency caused by oxygen-rich treatment was confirmed by the much smaller curvature radius of the $\text{Bi}_{24}\text{O}_{31}\text{Br}_{10}$ nanobelts and nanosheets compared to that of the BiOBr nanosheets. The curvature radius of the $\text{Bi}_{24}\text{O}_{31}\text{Br}_{10}$ nanobelts was even smaller than that of the $\text{Bi}_{24}\text{O}_{31}\text{Br}_{10}$ nanosheets, suggesting its higher charge separation efficiency. Moreover, the strongest photocurrent response of the nanobelts reveals its best performance of charge conversion (Fig. 9c). Therefore, the photogenerated e^- in the $\text{Bi}_{24}\text{O}_{31}\text{Br}_{10}$ nanobelts under visible light irradiation could be readily injected into the electrode, but recombine with the photogenerated h^+ with a difficulty. Thus, the nanobelts possessed a great charge

separation efficiency, which is in also favor of its photocatalytic pollutant degradation capacity.

3.7. Mechanisms behind the enhanced photocatalytic performance of $\text{Bi}_{24}\text{O}_{31}\text{Br}_{10}$ nanobelts

To deeply explore the influence of surface state of oxygen-rich bismuth oxyhalide on the photocatalytic degradation capacity, the electronic structure of (117) surface of the $\text{Bi}_{24}\text{O}_{31}\text{Br}_{10}$ nanobelts were compared with that of (001) surface of BiOBr. The calculated DOS and their projected DOS (PDOS) of BiOBr (001) and $\text{Bi}_{24}\text{O}_{31}\text{Br}_{10}$ (117) are shown in Fig. 10. Since the limitations of the DFT method, the theoretical values of semiconductor band gaps always tend to be underestimated [14,56,57]. The scissor operator can effectively figure out the difference between the theoretical and experimental band gaps to reflect the relative changes in electronic structure of oxygen-rich bismuth oxyhalide [57–59]. After taking into account the scissor of 0.505 eV for BiOBr (001) and 2.296 eV for $\text{Bi}_{24}\text{O}_{31}\text{Br}_{10}$ (117), the calculated band gaps matched well with the experimental values. Thus, these scissors were used to evaluate the DOS and PDOS. The zero point on the energy axis of the plots corresponds to the Fermi level. For the (117) facet of $\text{Bi}_{24}\text{O}_{31}\text{Br}_{10}$, the whole DOS moves to the lower energy level, accompanied with narrower band gap and the improvement of the visible light absorption capacity compared to the (001) facet of BiOBr. For instance, the Br 4p state at the VB moves to the lower energy level in the $\text{Bi}_{24}\text{O}_{31}\text{Br}_{10}$ (117) facet (Fig. 10b), forming a more stable structure of the photocatalytic structure. Due to the content of the O atoms in bismuth oxybromide increases, more states become available for occupation. The CB of bismuth oxybromide is mainly composed of a mixture of Bi 6p and O 2p orbitals. For $\text{Bi}_{24}\text{O}_{31}\text{Br}_{10}$ (117) facet, more percentage of O 2p states at conduction band minimum shifted to the negative energy level mainly results in the narrower band gap by comparing with the BiOBr (001) facet [59]. Therefore, the nanobelts tended to generate $\cdot\text{OH}$ and thus showed a better performance of visible-light-driven photocatalytic degradation.

On the basis of these aforementioned results, the mechanism for the photocatalytic degradation of BPA over the $\text{Bi}_{24}\text{O}_{31}\text{Br}_{10}$ nanobelts under visible light irradiation was elucidated and is shown in Fig. 11. First, the $\text{Bi}_{24}\text{O}_{31}\text{Br}_{10}$ nanobelts efficiently absorbed visible light because of its narrowed band gap. Then the separation of photogenerated

$h^+ - e^-$ pairs took place. After that, because the VB top position of the $\text{Bi}_{24}\text{O}_{31}\text{Br}_{10}$ nanobelts was sufficiently positive, the photogenerated h^+ in the VB could directly oxidize H_2O and form large quantities of free radicals. In this way, BPA molecules were degraded by these free radicals, and finally mineralized into CO_2 and H_2O .

4. Conclusions

In this work, $\text{Bi}_{24}\text{O}_{31}\text{Br}_{10}$ nanobelts were obtained using a simple hydrothermal route. The photocatalytic efficiency of the $\text{Bi}_{24}\text{O}_{31}\text{Br}_{10}$ nanobelts for BPA degradation was 4.3 and 4.0 times higher than those of the $\text{Bi}_{24}\text{O}_{31}\text{Br}_{10}$ and BiOBr nanosheets, respectively. More importantly, the $\text{Bi}_{24}\text{O}_{31}\text{Br}_{10}$ nanobelts could resist most interfering ions and efficiently treat actual industrial wastewaters. The experimental and DFT calculation results clearly indicate that the band gap of the nanobelts was sufficiently narrow and the VB top position was sufficiently positive. As a result, the $\text{Bi}_{24}\text{O}_{31}\text{Br}_{10}$ nanobelts exhibited a strong response to visible light and produced large quantities of $\cdot\text{OH}$ directly through its photogenerated h^+ , which is superior to the indirect $\cdot\text{OH}$ generation pathway over other photocatalysts like the $\text{Bi}_{24}\text{O}_{31}\text{Br}_{10}$ and BiOBr nanosheets. Therefore, effective photocatalytic degradation and mineralization of pollutants using visible light can be accomplished using bismuth oxybromide nanomaterials with morphology design and band structure modification.

Acknowledgments

The authors thank the National Natural Science Foundation of China (21590812 and 51538011), the Collaborative Innovation Center of Suzhou Nano Science and Technology of the Ministry of Education of China for supporting this work. The numerical calculations were performed on the supercomputing system in the Supercomputing Center at the University of Science and Technology of China, China.

Appendix A. Supplementary data

Supplementary material related to this article can be found, in the online version, at doi:<https://doi.org/10.1016/j.apcatb.2018.06.015>.

References

- [1] C.Y. Wang, X. Zhang, X.N. Song, W.K. Wang, H.Q. Yu, *ACS Appl. Mater. Interfaces* 8 (2016) 5320–5326.
- [2] C.Y. Wang, X. Zhang, H.B. Qiu, W.K. Wang, G.X. Huang, J. Jiang, H.Q. Yu, *Appl. Catal. B: Environ.* 200 (2017) 659–665.
- [3] D.A. Crain, M. Eriksen, T. Iguchi, S. Jobling, H. Laufer, G.A. LeBlanc, L.J. Guillette Jr., *Reprod. Toxicol.* 24 (2007) 225–239.
- [4] H. Li, J. Shang, Z. Ai, L. Zhang, *J. Am. Chem. Soc.* 137 (2015) 6393–6399.
- [5] M. Guan, C. Xiao, J. Zhang, S. Fan, R. An, Q. Cheng, J. Xie, M. Zhou, B. Ye, Y. Xie, *J. Am. Chem. Soc.* 135 (2013) 10411–10417.
- [6] J. Li, K. Zhao, Y. Yu, L. Zhang, *Adv. Funct. Mater.* 25 (2015) 2189–2201.
- [7] L. Ye, J. Liu, C. Gong, L. Tian, T. Peng, L. Zan, *ACS Catal.* 2 (2012) 1677–1683.
- [8] Y. Lu, H. Yu, S. Chen, X. Quan, H. Zhao, *Environ. Sci. Technol.* 46 (2012) 1724–1730.
- [9] J. Kim, C. Lee, W. Choi, *Environ. Sci. Technol.* 44 (2010) 6849–6854.
- [10] X. Zhang, L.W. Wang, C.Y. Wang, W.K. Wang, Y.L. Chen, Y.X. Huang, W.W. Li, Y.J. Feng, H.Q. Yu, *Chem. Eur. J.* 21 (2015) 11872–11877.
- [11] J. Li, L. Cai, J. Shang, Y. Yu, L. Zhang, *Adv. Mater.* 28 (2016) 4059–4064.
- [12] L. Sun, L. Xiang, X. Zhao, C.-J. Jia, J. Yang, Z. Jin, X. Cheng, W. Fan, *ACS Catal.* 5 (2015) 3540–3551.
- [13] J. Li, H. Li, G. Zhan, L. Zhang, *Acc. Chem. Res.* 50 (2017) 112–121.
- [14] A.M. Ganose, M. Cuff, K.T. Butler, A. Walsh, D.O. Scanlon, *Chem. Mater.* 28 (2016) 1980–1984.
- [15] J. Li, Y. Yu, L. Zhang, *Nanoscale* 6 (2014) 8473–8488.
- [16] Y. Ao, K. Wang, P. Wang, C. Wang, J. Hou, *Appl. Catal. B: Environ.* 194 (2016) 157–168.
- [17] L. Ye, Y. Su, X. Jin, H. Xie, C. Zhang, *Environ. Sci.: Nano* 1 (2014) 90–112.
- [18] X. Zhang, C.Y. Wang, L.W. Wang, G.X. Huang, W.K. Wang, H.Q. Yu, *Sci. Rep.* 6 (2016) 22800–22809.
- [19] H. Feng, Z. Xu, L. Wang, Y. Yu, D. Mitchell, D. Cui, X. Xu, J. Shi, T. Sannomiya, Y. Du, W. Hao, S.X. Dou, *ACS Appl. Mater. Interfaces* 7 (2015) 27592–27596.
- [20] L. Zhang, Z. Han, W. Wang, X. Li, Y. Su, D. Jiang, X. Lei, S. Sun, *Chem. Eur. J.* 21 (2015) 18089–18094.
- [21] Y.F. Fang, Y.P. Huang, J. Yang, P. Wang, G.W. Cheng, *Environ. Sci. Technol.* 45 (2011) 1593–1600.
- [22] Z. Ai, W. Ho, C. Lee, L. Zhang, *Environ. Sci. Technol.* 43 (2009) 4143–4150.
- [23] H. Yu, C. Cao, X. Wang, J. Yu, *J. Phys. Chem. C* 121 (2017) 13191–13201.
- [24] Y. Huo, J. Zhang, M. Miao, Y. Jin, *Appl. Catal. B: Environ.* 111–112 (2012) 334–341.
- [25] D. Zhang, M. Wen, B. Jiang, G. Li, J.C. Yu, *J. Hazard. Mater.* 211–212 (2012) 104–111.
- [26] R. Hou, X. Chen, Y. Gao, H. Zhu, S. Li, H. Li, Y. Huo, *ChemistrySelect* 1 (2016) 1000–1003.
- [27] H. Wang, W. Zhang, X. Li, J. Li, W. Cen, Q. Li, F. Dong, *Appl. Catal. B: Environ.* 225 (2018) 218–227.
- [28] X. Dong, W. Zhang, Y. Sun, J. Li, W. Cen, Z. Cui, H. Huang, F. Dong, *J. Catal.* 357 (2018) 41–50.
- [29] L. Yu, X. Zhang, G. Li, Y. Cao, Y. Shao, D. Li, *Appl. Catal. B: Environ.* 187 (2016) 301–309.
- [30] L. Xiao, J. Jiang, L. Zhang, *Appl. Catal. B: Environ.* 142–143 (2013) 487–493.
- [31] Y. Myung, F. Wu, S. Banerjee, A. Stoica, H. Zhong, S.S. Lee, J. Fortner, L. Yang, P. Banerjee, *Chem. Mater.* 27 (2015) 7710–7718.
- [32] X. Xiao, C. Liu, R. Hu, X. Zuo, J. Nan, L. Li, L. Wang, *J. Mater. Chem.* 22 (2012) 22840–22843.
- [33] C. Liu, D. Zhang, *Chem. Eur. J.* 21 (2015) 1–10.
- [34] L.-C. Tien, Y.-L. Lin, S.-Y. Chen, *Mater. Lett.* 113 (2013) 30–33.
- [35] C.Y. Wang, X. Zhang, H.B. Qiu, G.X. Huang, H.Q. Yu, *Appl. Catal. B: Environ.* 205 (2017) 615–623.
- [36] F.T. Li, Q. Wang, J. Ran, Y.J. Hao, X.J. Wang, D. Zhao, S.Z. Qiao, *Nanoscale* 7 (2015) 1116–1126.
- [37] Y. Peng, P.-P. Yu, Q.-G. Chen, H.-Y. Zhou, A.-W. Xu, *J. Phys. Chem. C* 119 (2015) 13032–13040.
- [38] Z. Liu, J. Niu, P. Feng, Y. Zhu, *Ceram. Int.* 41 (2015) 4608–4615.
- [39] J. Shang, W. Hao, X. Lv, T. Wang, X. Wang, Y. Du, S. Dou, T. Xie, D. Wang, *J. Wang, ACS Catal.* 4 (2014) 954–961.
- [40] M.D. Segall, P.J.D. Lindan, M.J. Probert, C.J. Pickard, P.J. Hasnip, S.J. Clark, M.C. Payne, *J. Phys.: Condens. Matter* 14 (2002) 2717–2744.
- [41] J.P. Perdew, K. Burke, M. Ernzerhof, *Phys. Rev. Lett.* 77 (1996) 3865–3868.
- [42] B.G. Pfrommer, M. Cote, S.G. Louie, M.L. Cohen, *J. Comput. Phys.* 131 (1997) 233–240.
- [43] N. Zhang, X. Li, H. Ye, S. Chen, H. Ju, D. Liu, Y. Lin, W. Ye, C. Wang, Q. Xu, J. Zhu, L. Song, J. Jiang, Y. Xiong, *J. Am. Chem. Soc.* 138 (2016) 8928–8935.
- [44] H. Wang, D. Yong, S. Chen, S. Jiang, X. Zhang, W. Shao, Q. Zhang, W. Yan, B. Pan, Y. Xie, *J. Am. Chem. Soc.* 140 (2018) 1760–1766.
- [45] D. Yue, T. Zhang, M. Kan, X. Qian, Y. Zhao, *Appl. Catal. B: Environ.* 183 (2016) 1–7.
- [46] M. Pan, H. Zhang, G. Gao, L. Liu, W. Chen, *Environ. Sci. Technol.* 49 (2015) 6240–6248.
- [47] C. Chang, L. Zhu, Y. Fu, X. Chu, *Chem. Eng. J.* 233 (2013) 305–314.
- [48] J. Jiang, K. Zhao, X. Xiao, L. Zhang, *J. Am. Chem. Soc.* 134 (2012) 4473–4476.
- [49] J. Li, Dong, Y. Sun, W. Cen, F. Dong, *Appl. Catal. B: Environ.* 226 (2018) 269–277.
- [50] L. Ye, J. Liu, Z. Jiang, T. Peng, L. Zan, *Appl. Catal. B: Environ.* 142–143 (2013) 1–7.
- [51] Y. Mi, L. Wen, Z. Wang, D. Cao, R. Xu, Y. Fang, Y. Zhou, Y. Lei, *Nano Energy* 30 (2016) 109–117.
- [52] S. Ning, L. Ding, Z. Lin, Q. Lin, H. Zhang, H. Lin, J. Long, X. Wang, *Appl. Catal. B: Environ.* 185 (2016) 203–212.
- [53] J. Barreto, G. Smith, N. Strobel, P. McQuillin, T. Miller, *Life Sci.* 56 (1995) 89–96.
- [54] F. Wang, T.A. Shifa, X. Zhan, Y. Huang, K. Liu, Z. Cheng, C. Jiang, J. He, *Nanoscale* 7 (2015) 19764–19788.
- [55] F. Wang, S. Wei, Z. Zhang, G.R. Patzke, Y. Zhou, *Phys. Chem. Chem. Phys. : PCCP* 18 (2016) 6706–6712.
- [56] X.B. Chen, L. Liu, P.Y. Yu, S.S. Mao, *Science* 331 (2011) 746–750.
- [57] E. Zahedi, *Superlatt. Microstruct.* 81 (2015) 49–63.
- [58] W.-J. Yin, H. Tang, S.-H. Wei, M.M. Al-Jassim, J. Turner, Y. Yan, *Phys. Rev. B* 82 (2010) 45106–45111.